

GaN/AlGaN intersubband optoelectronic devices

This content has been downloaded from IOPscience. Please scroll down to see the full text.

2009 New J. Phys. 11 125023

(<http://iopscience.iop.org/1367-2630/11/12/125023>)

View [the table of contents for this issue](#), or go to the [journal homepage](#) for more

Download details:

IP Address: 103.21.125.82

This content was downloaded on 11/01/2017 at 17:15

Please note that [terms and conditions apply](#).

You may also be interested in:

[III-nitride semiconductors for intersubband optoelectronics: a review](#)

M Beeler, E Trichas and E Monroy

[Photodetectors based on intersubband transitions using III-nitride superlattice structures](#)

Daniel Hofstetter, Esther Baumann, Fabrizio R Giorgetta et al.

[Recent progress in quantum cascade lasers and applications](#)

Claire Gmachl, Federico Capasso, Deborah L Sivco et al.

[Current status of AlInN layers lattice-matched to GaN for photonics and electronics](#)

R Butté, J-F Carlin, E Feltin et al.

[Resonant tunneling transport in Al_zGa_{1-z}N/In_xGa_{1-x}N/Al_zGa_{1-z}N/In_yGa_{1-y}N quantum structures](#)

A Bhour, A Rached and J-L Lazzari

[Nonpolar m-plane GaN/AlGaN heterostructures with intersubband transitions in the 5–10 THz band](#)

C B Lim, A Ajay, C Bougerol et al.

[Intersubband all-optical switching based on Coulomb-induced optical nonlinearities](#)

Y Li and R Paiella

[Resonant Tunneling Transport in a GaN/AlN Multiple-Quantum-Well Structure](#)

Salam Sakr, Yulia Kotsar, Maria Tchernycheva et al.

[Novel InP- and GaSb-based light sources for the near to far infrared](#)

Spengel Stephan, Demmerle Frederic and Amann Markus-Christian

GaN/AlGaN intersubband optoelectronic devices

H Machhadani¹, P Kandaswamy², S Sakr¹, A Vardi³,
A Wirtmüller², L Nevou¹, F Guillot², G Pozzovivo⁴,
M Tchernycheva¹, A Lupu¹, L Vivien¹, P Crozat¹, E Warde¹,
C Bougerol², S Schacham³, G Strasser⁴, G Bahir³,
E Monroy² and F H Julien^{1,5}

¹ Institut d'Electronique Fondamentale, UMR CNRS 8622,
University Paris-Sud XI, 91405 Orsay, France

² Equipe mixte CEA-CNRS Nanophysique et Semiconducteurs,
INAC/SP2M/PSC, CEA, 17 rue des Martyrs, 38054 Grenoble Cedex 9, France

³ Department of Electrical Engineering, Technion-Israel Institute of
Technology, Haifa 32000, Israel

⁴ Zentrum für Mikro und Nanostrukturen, Technical University Vienna
Floragasse 7, A-1040 Vienna, Austria

E-mail: francois.julien@u-psud.fr

New Journal of Physics **11** (2009) 125023 (16pp)

Received 3 October 2009

Published 17 December 2009

Online at <http://www.njp.org/>

doi:10.1088/1367-2630/11/12/125023

Abstract. This paper reviews recent progress toward intersubband (ISB) devices based on III-nitride quantum wells (QWs). First, we discuss the specific features of ISB active region design using GaN/AlGaN materials, and show that the ISB wavelength can be tailored in a wide spectral range from near- to long infrared wavelengths by engineering the internal electric field and layer thicknesses. We then describe recent results for electro-optical waveguide modulator devices exhibiting a modulation depth as large as 14 dB at telecommunication wavelengths. Finally, we address a new concept of III-nitride QW detectors based on the quantum cascade scheme, and show that these photodetectors offer the prospect of high-speed devices at telecommunication wavelengths.

⁵ Author to whom any correspondence should be addressed.

Contents

1. Introduction	2
2. III-nitride ISB transitions	3
2.1. Design of ISB heterostructures	3
2.2. Scaling laws of the ISB wavelength in the near-infrared spectral range	5
2.3. Toward long infrared wavelength ISB devices	6
3. III-nitride electro-optical modulators	8
4. High-performance quantum cascade detectors (QCDs)	10
5. Conclusion and prospects	14
Acknowledgments	15
References	15

1. Introduction

Intersubband (ISB) transitions are resonant optical transitions between the confined states of semiconductor heterostructures, either in the conduction or the valence band [1]. They have been thoroughly studied in the past 20 years because they offer fascinating possibilities for control-by-design devices relying on quantum wells (QWs) or quantum dots (QDs). One famous example is the quantum cascade laser (QCL), which was invented in the mid-1990s at Bell Laboratories [2]. Using materials such as GaAs/AlGaAs, InGaAs/AlInAs or antimonides, ISB devices such as the QCLs can be tuned from the mid-infrared to the THz spectral range. Operation at short wavelengths is limited by the available conduction band offset and by the material transparency. III-nitride semiconductors (GaN, AlN, InN and their alloys) are attracting much interest for ISB devices operating in the near-infrared spectral range and, in particular, in the 1.3–1.55 μm wavelength window used for fiber optic telecommunications. Not only are they transparent in a wide spectral region (360 nm to 13 μm for GaN), but the conduction band offset provided by their heterostructures is quite large, being of the order of 1.75 eV for GaN/AlN [3]. In contrast to InAs/AlSb materials, which also exhibit a large conduction band discontinuity, the remote valleys of GaN lie very high in energy (> 2 eV above the Γ point [4]), offering the potential for ISB light-emitting devices at record short near-infrared wavelengths. Another specificity of nitride materials is substantial longitudinal-optical (LO) phonon energy (92 meV for GaN), as well as the presence of huge internal fields induced by spontaneous and piezoelectric polarizations along the c -axis, inherent in their wurtzite structure. Due to the rather heavy electron effective mass ($0.22 \times m_0$ for GaN), ultrathin QW or QD layers, typically 1–1.5 nm thick, are required in order to tune the ISB wavelength in the 1.3–1.55 μm range.

Short-wavelength ISB absorption has been reported by several groups in GaN/AlGaIn multi-QW structures [5]–[9] and coupled QWs [10, 12], as well as lattice-matched GaN/AlInN and strain-compensated GaInN/AlInN QWs [13, 14]. Intraband absorption at telecommunication wavelengths has also been observed at room temperature in self-organized GaN/AlN QDs [15]–[17]. Although much progress has been recently achieved using ammonia-source molecular beam epitaxy [18], plasma-assisted molecular beam epitaxy (PAMBE) is best suited for growing short-wavelength nitride-based ISB devices because of its inherently low growth temperature and slow growth rate, which allows accurate control of layer thickness and interface abruptness down to one monolayer (1 ML = 0.2593 nm in relaxed GaN) [19].

The growth of ultrathin layers with sharp interfaces using metal-organic vapor phase epitaxy (MOVPE) has been challenging, because of interface instabilities induced by high growth temperature and built-in strain [20]–[24].

One key feature of nitride-based ISB transitions is the extremely short absorption recovery time (measured in the 150–400 fs range) as a consequence of very efficient ISB scattering processes involving LO-phonons in these highly polar materials [25]–[27]. This offers the prospect of ultrafast ISB devices operating at multi-Tbit s⁻¹ data rates. All-optical switches based on ISB absorption saturation have been demonstrated with control switching energy as low as 38 pJ for 10 dB contrast [28, 29]. These ultrafast all-optical devices are of great interest for optical time division multiplexed systems. Applications for photodetection have also been investigated. Both photovoltaic and photoconductive GaN/AlN QW detectors have been demonstrated [30, 31]. Because of the large density of threading dislocations, typical of III-nitride layers grown on foreign substrates (10^9 – 10^{10} cm⁻²), photoconductive QW detectors exhibit a large dark current. It was shown that in the case of photovoltaic devices, detection arises from nonlinear optical rectification processes with, as a consequence, rather low sensitivity [31]. Nitride-based QD photodetectors relying on in-plane transport have also been demonstrated in the 1.3–1.55 μ m wavelength range at room temperature [32, 33]. Electro-optical modulation devices operating at telecommunication wavelengths have also recently been reported. They rely on the charge transfer between a two-dimensional (2D) electron gas and a superlattice [34], or on electron tunneling between two coupled GaN/AlN QWs [35, 36]. In terms of optoelectronic technology, low-loss III-nitride-based optical waveguides have been demonstrated at telecommunication wavelengths [37, 38]. Room-temperature ISB light emission at a near-infrared wavelength of $\approx 2 \mu$ m has been reported in GaN/AlN QWs under continuous wave optical excitation [39]–[41], and more recently using optical pumping by a pulsed OPO source [42]. Intraband emission at 1.5 μ m wavelength from GaN/AlN QDs has been observed at room temperature using resonant Raman excitation [43, 44]. It was also shown that III-nitride ISB structures exhibit enhanced second-harmonic and third-order optical nonlinearities [45, 46].

In this paper, we first describe the design and characterization of GaN-based structures for ISB absorption. We show that the ISB wavelength can be tuned in the near- to mid-infrared spectral range by engineering the electron quantum confinement and internal field. We then illustrate the recent achievements of III-nitride ISB devices, starting with an electro-optical waveguide modulator exhibiting 14 dB modulation depth at telecommunication wavelengths. After that we focus on a new concept of III-nitride based QW detectors, reliant on the quantum cascade scheme, and show that these devices offer high-frequency operation at telecommunication wavelengths [47, 48].

2. III-nitride ISB transitions

2.1. Design of ISB heterostructures

Unlike standard ISB material systems such as GaAs/AlGaAs, InGaAs/InAlAs and InAs/AlSb, III-nitride semiconductors preferentially crystallize in the wurtzite structure. Even for an ideal wurtzite structure, the barycenters of positive and negative charges, respectively, carried by the group III and the group V atoms do not coincide along the *c*-axis [0001]. As a consequence, III-nitride materials exhibit spontaneous polarization (pyroelectric effect). In addition, depending on the strain state of the layers, an additional negative or positive contribution to

the total polarization appears, due to the piezoelectric effect. In the form of heterostructures, the polarization discontinuity between the well and barrier materials gives rise to bound charges of opposite sign at each interface, and hence to an internal electric field of opposite sign in the well and barrier layers. For a thin layer of GaN within an AlN matrix, it was shown that the internal field in the GaN well can be as large as 10 MV cm^{-1} [3]. This polarization discontinuity has major consequences for the design of III-nitride ISB devices. It dictates the ISB transition energy for thick enough QWs, but it also leads to strong band bending effects, as well as the formation of a depletion layer and of an accumulation layer with a 2D electron gas at the edges of the active region. In addition, it has major consequences for the distribution of carriers within the active layers.

We first consider the effect on the band profile of the **doping concentration and of the composition of the cladding layers**. The simulated structure is a 10-period superlattice with **2 nm thick GaN wells** and **2 nm thick AlN barriers** sandwiched between top and bottom layers consisting of either GaN, AlN or $\text{Al}_{0.5}\text{Ga}_{0.5}\text{N}$. The calculation was performed using a Schrödinger–Poisson solver (C-Band), accounting for the known material data [49] and assuming Fermi level pinning at the surface. All materials are assumed to have metal polarity, i.e. growth along the [0001] crystallographic axis. Figure 1 shows the band profile and the electron concentration for GaN claddings (figures 1(a)–(c)), AlN claddings (figures 1(d) and (e)), top AlN and bottom GaN claddings (figure 1(f)), and $\text{Al}_{0.5}\text{Ga}_{0.5}\text{N}$ claddings (figures 1(g)–(i)). The claddings are either non-intentionally doped or n-doped at a concentration of $1 \times 10^{19} \text{ cm}^{-3}$. For figures 1(a), (d), (g) and (h), the active wells are undoped. For all other cases, the GaN wells are n-doped at a concentration of $5 \times 10^{19} \text{ cm}^{-3}$.

For GaN cladding layers, a **2D electron gas forms at the interface between the bottom cladding and the active region**, while a depletion layer develops at the interface between the top cladding and the active region. In the case of AlN claddings, band bending occurs in the opposite direction and a depletion layer develops at the interface between the bottom cladding and the active region. As expected when both the claddings and GaN wells are undoped, the active region is fully depleted of electrons. For undoped GaN claddings (figure 1(b)), the wells become populated with electrons when the active region is doped at a concentration exceeding $2 \times 10^{19} \text{ cm}^{-3}$. Note that this value is given only as a reference, being a function of the top cladding thickness and the number of QWs in the active region. For GaN claddings and doped GaN wells, the three QWs closer to the surface are fully depleted of electrons (see figures 1(b) and (c)). Doping of the GaN claddings at $1 \times 10^{19} \text{ cm}^{-3}$ does not improve the electron concentration in the wells, which in addition becomes inhomogeneously distributed (figure 1(c)). For an active region grown on doped GaN claddings with an AlN cap layer, the electron concentration profile in the active region is also inhomogeneous. Only for doped $\text{Al}_{0.5}\text{Ga}_{0.5}\text{N}$ claddings (figure 1(i)) is the band profile almost flat across the active region and doping of the GaN wells efficient, resulting in a homogeneous electron concentration profile. Interestingly, as seen in figure 1(h), for doped AlGaN claddings the active region is weakly populated with electrons, even if the active region is undoped. In summary, good control of the electron population in the active region is only achieved with doped AlGaN claddings. The most effective situation is obtained when the Al content of the doped claddings corresponds to the average Al content of the superlattice.

One common approximation for designing ISB III-nitride devices is to assume periodic potential conditions to calculate the transition energies. In this approximation, the potential drop across one period of the superlattice is zero. This approximation is justified for a majority

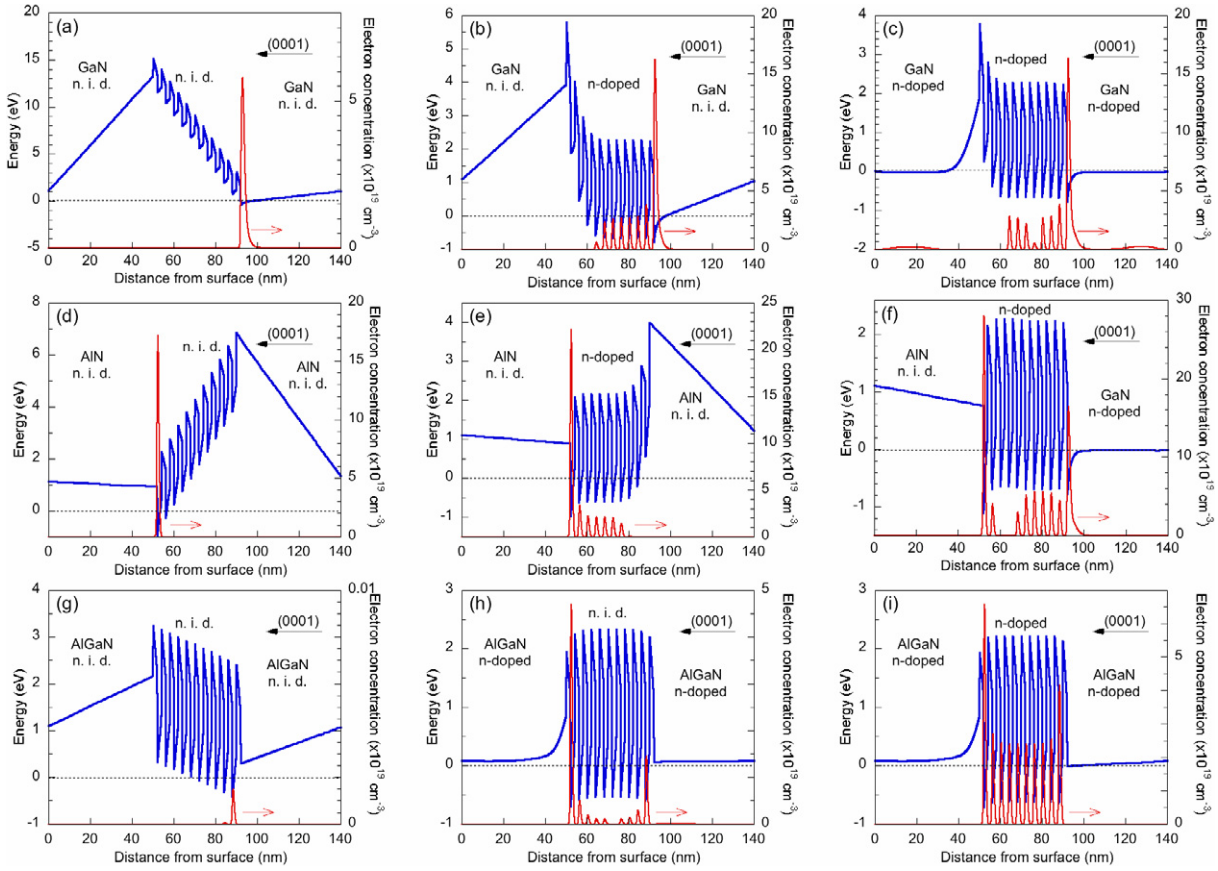


Figure 1. Conduction band profile and electron concentration for a 10-period GaN/AlN superlattice sandwiched between GaN claddings (a–c), AlN claddings (d, e), AlN top and GaN bottom claddings (f), and $\text{Al}_{0.5}\text{Ga}_{0.5}\text{N}$ claddings (g–i). For (a), (b), (d), (e) and (g), the claddings are undoped. For (c), (h) and (i), the claddings are n-doped at a concentration of $1 \times 10^{19} \text{ cm}^{-3}$. For (f), only the bottom cladding is n-doped. The active region is undoped for (a), (d), (g) and (h). For (b), (c), (e), (f) and (i), the GaN wells are n-doped at a concentration of $5 \times 10^{19} \text{ cm}^{-3}$. The dotted line corresponds to the Fermi energy.

of QWs within the active region, especially when both claddings are doped. The internal electric field in the well and barrier layers can then be easily calculated using the formula [50, 51]

$$F_w = \frac{P_b - P_w}{\epsilon_0} \frac{t_b}{\epsilon_{rw} t_w + \epsilon_{rb} t_b}, \quad F_b = F_w \frac{t_w}{t_b}, \quad (1)$$

where ‘w’ and ‘b’ stand, respectively, for the well and barrier materials, P is the algebraic sum of the spontaneous and piezoelectric polarizations, t is the layer thickness, ϵ_0 is the vacuum permittivity and ϵ_r is the relative permittivity.

2.2. Scaling laws of the ISB wavelength in the near-infrared spectral range

Figure 2 shows the ISB transition energy calculated using an 8-band k.p model for a superlattice with GaN wells and 3 nm thick AlN barriers assuming periodic conditions. The curves are the

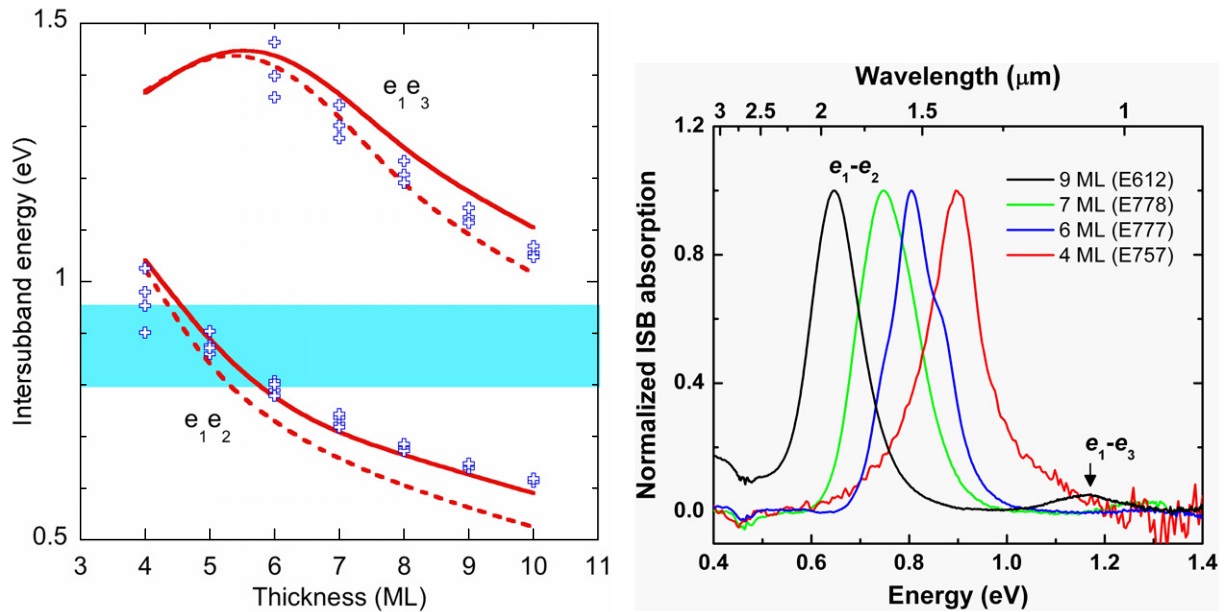


Figure 2. Left: ISB transition energies calculated for a periodic GaN/AlN superlattice with 3 nm thick AlN barriers as a function of the number of atomic monolayers of the GaN wells. The solid (dashed) curve is the simulation assuming that the superlattice is strained on GaN (AlN). The crosses are experimental data. Right: measured ISB absorption spectra at room temperature of representative samples with well thicknesses of 4, 6, 7 and 9 ML.

results of a simulation assuming that the superlattice is strained on GaN or AlN. The dots are the results of ISB spectroscopic measurements performed on 20 period superlattices grown by PAMBE on AlN-on-sapphire (0001) templates [3]. Details of the sample structures and growth procedure can be found in [52]. As seen in figure 2, the e_1e_2 transition energy covers the spectral range used for fiber-optic telecommunication for a GaN well thickness comprised between 4 and 6 ML (1–1.5 nm).

Two regimes can be distinguished. For well thicknesses below 6 ML, both the e_1 and e_2 states are confined by the two interfaces, which means that the transition energy is mostly governed by the well thickness, i.e. by the quantum size effect. In turn, for well thicknesses above 7 ML, the ground and excited states are confined by the V-shaped potential in the GaN well. The transition energy is therefore ruled by the magnitude of the internal field. For thick enough QWs, an ISB absorption from the ground state to the e_3 excited state is also observed. This transition is allowed by the built-in asymmetric potential. The e_1e_3 absorption vanishes when the well thickness is reduced because of the delocalization of the e_3 state in the barrier layers and the consequent reduction of the associated oscillator strength.

2.3. Toward long infrared wavelength ISB devices

The substantial energy of LO-phonons in GaN (92 meV) offers the prospect of ISB devices at wavelengths inaccessible to other III–V semiconductors because of their Reststrahlen absorption band. In addition, this substantial LO-phonon energy could be a key factor in view

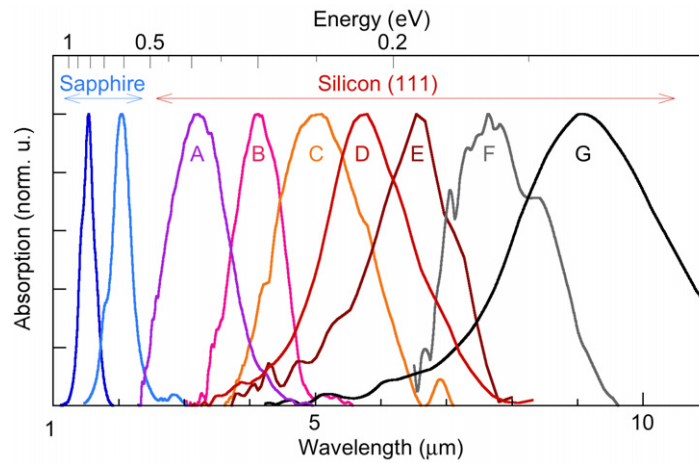


Figure 3. Infrared absorption spectra for TM-polarized light measured in GaN/AlGa_N superlattices with different barrier Al contents and QW width, grown either on sapphire or on Si(111) templates.

Table 1. Nominal growth parameters, ISB peak energy and FWHM of samples A–G.

Sample	Barrier/well thickness (nm)	Al (%)	ISB energy (wavelength) (meV (μm))	FWHM (meV)
A	3/3	60	384 (3.22)	123
B	3/3	40	299 (4.14)	53
E	3/3	35	277 (4.47)	49
F	3/3	30	268 (4.63)	43
C	3/3	20	243 (5.10)	61
D	3/5	35	218 (5.69)	48
E	3/5	20	185 (6.67)	35
F	4/6	10	162 (7.64)	29
G	4/7	10	136 (9.08)	34

of the high temperature operation of future III-nitride THz QCLs. In order to tune the III-nitride ISB transitions to long wavelengths, the internal field in the GaN wells must be reduced. Based on equation (1), this can be done by employing low aluminum content in the barrier materials and by reducing the barrier thickness with respect to the well thickness.

Figure 3 shows the ISB absorption spectra at room temperature of 40-period superlattice samples with 1–7 nm thick GaN wells and AlGa_N barriers with an Al concentration varying from 100% down to 10%. Both the GaN and the Al_xGa_{1-x}N layers were grown by PAMBE under Ga excess conditions at a temperature of 700 °C—about 20 °C below the GaN/AlN superlattice standard growth temperature—in order to obtain sharp interfaces and minimize alloy diffusion [53]. Before the growth of the active region, a buffer structure consisting of 150 nm of GaN and 150 nm of Al_xGa_{1-x}N was deposited. Since the transparency of sapphire vanishes at wavelengths above 5 μm, high-resistivity Si(111) templates were used for the growth of the long wavelength ISB structures. The nominal parameters are shown in table 1.

As seen in figure 3, by reducing the Al content of the barriers from 60% down to 10% and increasing the barrier thickness with respect to the well thickness, the peak ISB wavelength can be tuned in the range 3.2–9 μm . In the wavelength plot of figure 3, the ISB linewidth could wrongly appear to be increasing with the peak wavelength. In fact, the broadening factor $\Delta\lambda/\lambda$ is of the order of 20% for most spectra. Part of the broadening can be accounted for by variation of the internal field inside the GaN wells induced by monolayer fluctuations of the well and barrier thickness. Finally, it should be noted that, in order to reach the long-wavelength infrared spectral region, alternative approaches could be used, aimed at minimizing or even suppressing the internal field along the c -axis. This, for example, could be achieved by implementing the growth of semi-polar or non-polar wurtzite or even cubic III-nitride materials [54, 55].

3. III-nitride electro-optical modulators

Electro-optical modulators are key devices for fiber-optic telecommunications technology. The first electro-optical modulator based on ISB transitions in GaN/AlN QWs was proposed by P. Holmstrom in 2006 [56]. The device relies on the Stark shift of the ISB absorption under an applied bias. A frequency response as high as 60 GHz was predicted. It was also pointed out that ISB electro-optical modulators provide a better handling of chirp issues during the commutation process than their interband counterparts due to the resonant nature of the ISB transitions. Experimentally, nitride ISB modulators relying on bias control of the electron population of a superlattice under a Schottky contact were first demonstrated by [34]. Modulators based on electron tunneling in double GaN/AlN QWs coupled by a 4 ML thick AlN barrier have also been proposed and demonstrated [35]. The active structure of such a device consists of a wide well, which acts as an electron reservoir, and a narrow well designed to exhibit ISB absorption at 1.3–1.5 μm . By biasing the coupled QW structure, electrons are transferred from the reservoir well to the active well, which gives rise to electro-absorption at telecommunication wavelengths. An optical modulation bandwidth as high as 3 GHz was measured in $15 \times 15 \mu\text{m}^2$ mesa modulators [36]. The frequency response was shown to be extrinsically limited by the RC time constant of the device, where R is the resistance and C is the capacitance. It was foreseen that much higher optical modulation bandwidths could be achieved by reducing the device size and the resistivity of the contact layers since the main intrinsic limiting mechanism is the tunneling time between the two wells, which is estimated to be of the order of a few picoseconds. This miniaturization could be achieved by inserting the active region inside an optical waveguide. With respect to mesa modulators, which only allow a single pass of the optical beam through the active layers, optical waveguide modulators would, in addition, provide higher modulation depths as well as compatibility with current optical communication technologies.

In order to test the feasibility of an optical waveguide modulator, we designed a simplified electro-modulator structure. The sample was grown by PAMBE on a 1 μm thick AlN template on c -sapphire substrate. It consisted of three periods of 1.3 nm thick GaN wells with 3 nm thick AlN barriers. The wells were n-doped with Si at $2 \times 10^{19} \text{ cm}^{-3}$. The active region was sandwiched between two 500 nm thick $\text{Al}_{0.5}\text{Ga}_{0.5}\text{N}$ bottom and top contact layers n-doped with Si at $5 \times 10^{18} \text{ cm}^{-3}$. These layers also acted as confinement layers for the waveguide.

Chlorine inductively coupled plasma reactive ion etching (ICP–RIE) was used to fabricate 50 μm wide ridge waveguides. Ti/Al/Ni/Au metals were deposited to form the top and bottom contacts. The top contact was designed to cover only part of the ridge in order to minimize the

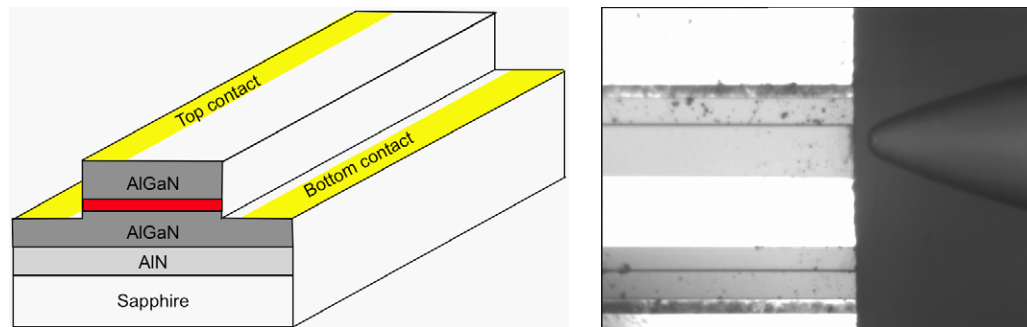


Figure 4. Left: sketch of the depletion waveguide modulator. Right: top microscope image of one waveguide device with the lensed optical fiber used for light injection. The white regions are the metallic contacts.

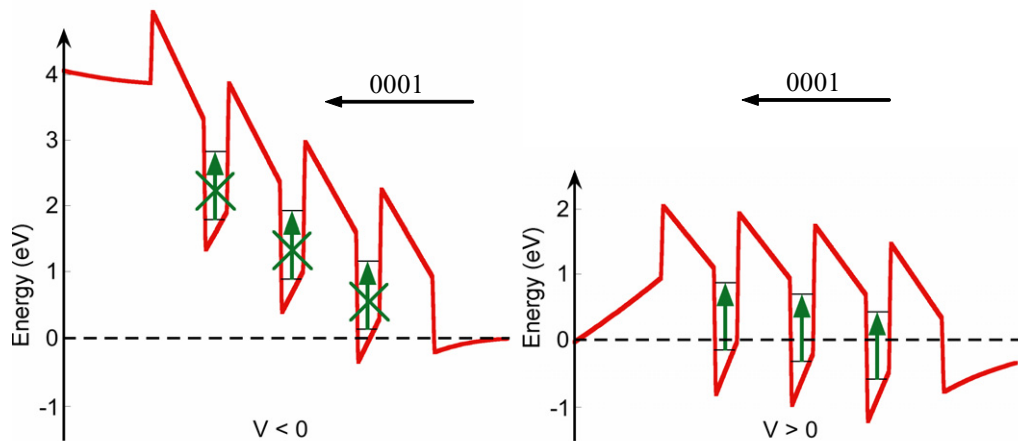


Figure 5. The principle of operation of the depletion modulator. The QWs are designed to exhibit ISB absorption at $1.5\ \mu\text{m}$ wavelength when populated with electrons. Under negative applied bias, the QWs are depleted and no absorption takes place, while under positive applied bias the electron population of the wells gives rise to ISB absorption at $1.5\ \mu\text{m}$ wavelength.

propagation losses due to plasmon absorption in the metal. The sample was then diced and the facets mechanically polished to form optical waveguides with a length of $1.675\ \text{mm}$. A sketch of the device is shown in figure 4.

The operating principle of the device is shown in figure 5. Under negative applied bias, the three QWs are depleted and the modulator is transparent, while under positive applied bias the electron population of the wells gives rise to ISB absorption at $1.5\ \mu\text{m}$ wavelength. Simulations show that at zero applied bias, the first well in growth order is populated, while the two other wells are depleted.

The waveguide samples were characterized using a semiconductor laser diode tunable in the $1.25\text{--}1.65\ \mu\text{m}$ wavelength range. A lensed optical fiber was used to couple the light into the waveguide modulators (see figure 4). The light transmitted through the waveguide was monitored using an infrared photodiode.

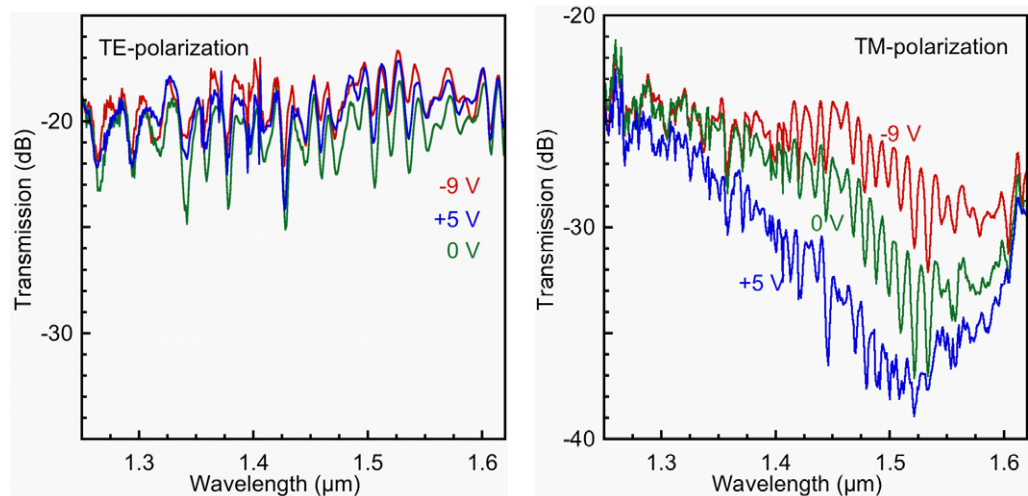


Figure 6. Waveguide transmission spectra for TE-polarized (left) and TM-polarized (right) light under an applied bias of -9 V, 0 V and 5 V, respectively.

Figure 6 presents the waveguide transmission spectrum at various applied biases for transverse electric-(TE) polarized (left) and transverse magnetic-(TM) polarized (right) light. The oscillations in the spectra are due to transverse mode beatings. For TE-polarized light, all waveguides show practically flat transmission in the 1.25 – 1.65 μm wavelength range. The transmission not corrected for the coupling losses is around -20 dBm and is found not to depend on the applied bias. This is not the case for TM-polarized light. The absorption increases when the bias is increased from -9 to $+5$ V as a result of the population of the ground state of the QWs. One can also notice a blue shift of the peak absorption wavelength with increasing biases, which can be attributed to a Stark shift of the ISB absorption. At zero bias, the modulator is absorbing, which result is in line with the simulations since one of the wells is expected to be populated.

Figure 7 shows the room-temperature transmission for TM-polarization of one of the waveguide devices versus the static applied bias. The transmission for TM-polarization is constant for negative voltage below -9 V because the three wells are depleted. It rapidly decreases when the voltage is increased from -9 to $+7$ V as a consequence of the increased ISB absorption resulting from the electron population of the QWs. The main result of figure 7 is the very large modulation depth, which is achieved by varying the applied bias. The modulation depth is of the order of 14 dB for -9 V/ $+6$ V applied bias and 10 dB for ± 5 V voltage swing. A value of 12 dB is required for optical modulators in order to achieve 10^{-12} bit error rates in current technology fiber optic data transmission systems. It should be noted that although the present prototype was not designed for high-speed operation, high modulation speeds could be achieved by optimizing the design of the structure.

4. High-performance quantum cascade detectors (QCDs)

QCDs are an appealing alternative to QW infrared photodetectors (QWIPs) [57]. In contrast to QWIPs, QCDs are photovoltaic devices and they can be operated at zero bias. Under illumination, electrons from the ground state are excited to the upper state of the active QW and

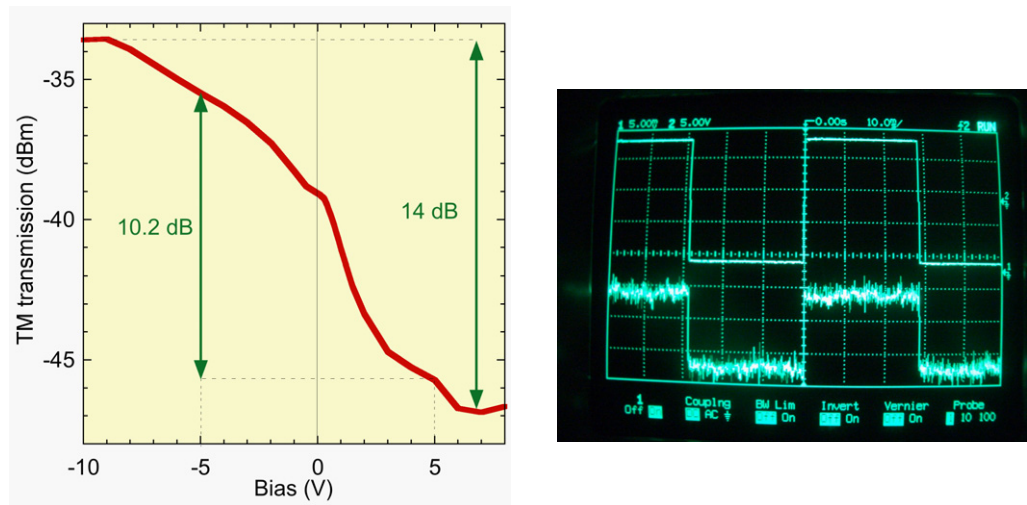


Figure 7. Left: transmission of the depletion modulator waveguide device versus static applied bias for TM-polarization. The transmission is not corrected for the coupling losses. Right: oscilloscope traces of the driving applied bias (top trace) and of the optical signal transmitted through the waveguide modulator (bottom trace).

then are transferred to an extractor region where they experience multiple relaxations toward the next active QW. This results in a macroscopic photovoltage in an open circuit configuration, or in a photocurrent if the device is loaded on a resistor. The dark current is extremely low, which is particularly favorable for enhancing the signal-to-noise ratio and improving the dynamic range and integration time of infrared imagers because the dark current does not saturate the read-out circuit [58]. QCDs have been demonstrated in several material systems, namely GaAs/AlGaAs, InGaAs/InAlAs and InGaAs/AlAsSb, operating at wavelengths as short as $2.1 \mu\text{m}$ [59]. Another appealing feature of QCDs is their intrinsically low capacitance, which enables high frequency response.

The GaN/AlGaN material system offers the prospect of QCDs operating at near-infrared wavelengths [47]. Figure 8 shows the conduction band profile of one period of the GaN/AlGaN QCD, as well as the sample structure. The active QW consists of an n-doped 6 ML thick GaN well with a 4 ML thick AlN barrier. The extractor is formed by a superlattice containing 4 ML thick $\text{Al}_{0.25}\text{Ga}_{0.75}\text{N}$ wells and 4 ML thick AlN barriers. Because of the polarization discontinuity between GaN, AlN and $\text{Al}_{0.25}\text{Ga}_{0.75}\text{N}$, band bending occurs in the extractor region, which results in an energy ladder of the ground states of the extractor QWs. The design was optimized to achieve an energy separation between the extractor ground states close to the LO-phonon energy.

The device was grown by PAMBE. It contains 40 periods of active regions between two $\text{Al}_{0.25}\text{Ga}_{0.75}\text{N}$ contact layers n-doped with silicon at $1 \times 10^{19} \text{ cm}^{-3}$. As shown in figure 8 (right), transmission electron microscopy (TEM) reveals abrupt interfaces as well as good reproducibility of the layer thickness.

Fourier transform infrared spectroscopy was performed at room temperature to analyze the ISB absorption spectrum of the sample in a multi-pass waveguide configuration. Figure 9 shows the absorption spectrum per one pass through the 40-period active region at room temperature.

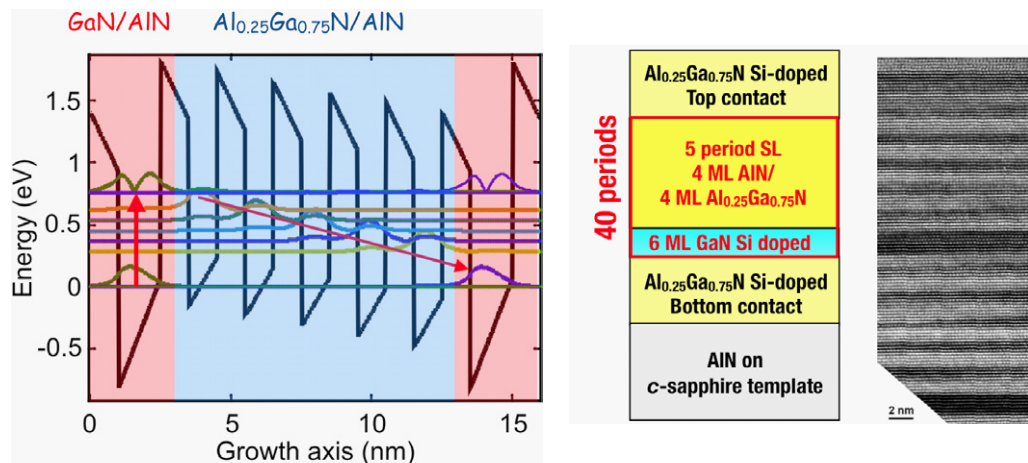


Figure 8. Left: conduction band profile of one period of a GaN/AlGaN QCD. Right: sample structure and TEM image of two periods of the active region.

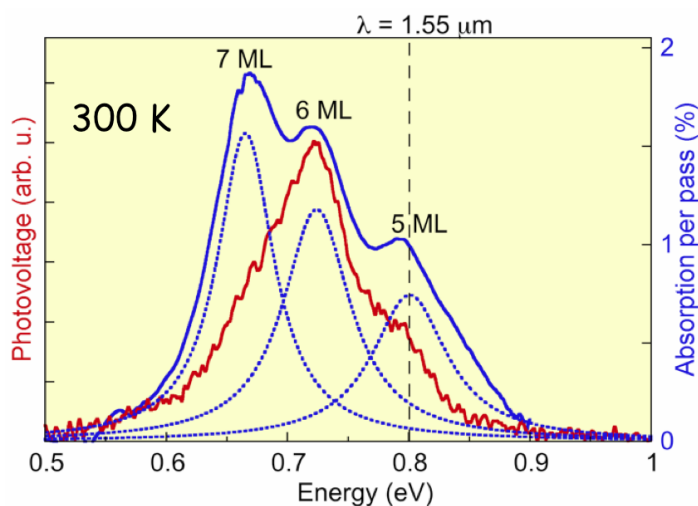


Figure 9. Room-temperature absorption and photovoltage spectrum of the QCD sample. The dotted curves are Lorentzian fits of the absorption spectrum.

The three peaks in the spectrum correspond to the absorption of an active QW with thicknesses of 5, 6 and 7 ML, respectively. The spectrum is perfectly fitted by the sum of three Lorentzian curves with an FWHM (full-width at half-maximum) of 65 meV. This structuration of the ISB absorption is typical of ultrathin GaN/AlN QWs [3]. It stems from the fact that the ISB energy shift induced by a 1 ML change of the well thickness is larger than the homogeneous broadening.

Figure 9 also shows the photovoltage spectrum measured at room temperature under TM-polarized irradiation. The photovoltage is at maximum at a wavelength of $1.7 \mu\text{m}$, which corresponds to an active QW thickness of 6 ML. The fact that the responsivity is smaller for a QW thickness of 5 or 7 ML can be understood as follows. For a 7 ML thickness of the active QW, simulations show that the excited state in the active QW lies at an energy 100 meV lower than that of the ground state of the first extractor well, while for a 5 ML thickness the excited state

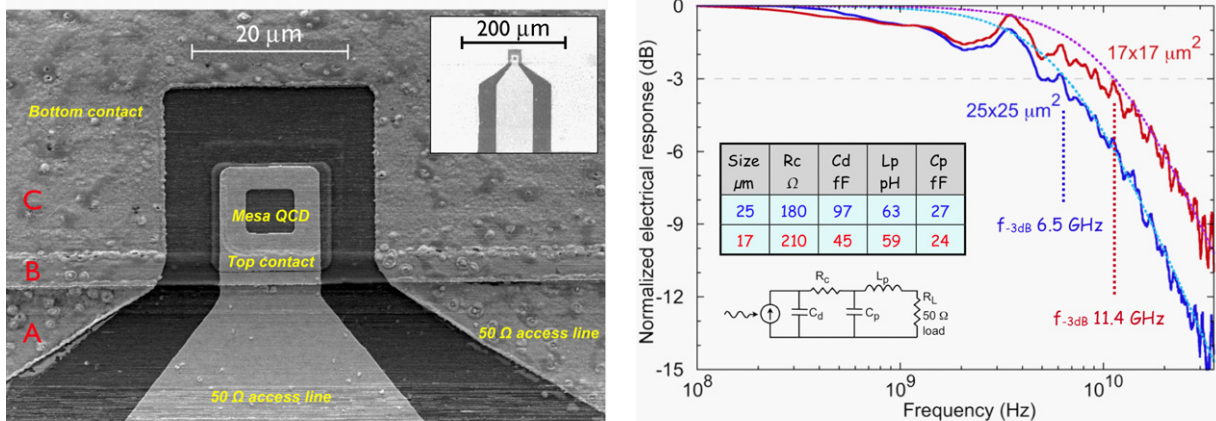


Figure 10. Left: scanning electron microscope images of a $17 \times 17 \mu\text{m}^2$ mesa QCD. Right: normalized frequency response ($20 \times \log(\text{photocurrent})$) for two mesa sizes. The full (dotted) curves are the measurements (simulations). The insets show the equivalent electrical circuit and the measured circuit parameters.

is 350 meV above the ground state energy of the first extractor well. In both cases, this results in a lower efficiency of the electron transfer from the active QW excited state into the extractor with respect to the ‘ideal’ situation shown in figure 8 corresponding to a 6 ML thick active QW. The peak responsivity was carefully calibrated at room temperature and was measured as $\sim 10 \text{ mA W}^{-1}$ ($\sim 1000 \text{ V W}^{-1}$) at $\lambda = 1.7 \mu\text{m}$ [47]. The responsivity decreases from its maximum value by a factor of ~ 3 at $\lambda = 1.5 \mu\text{m}$. Devices with an area of $A = 200 \times 200 \mu\text{m}^2$ exhibit a resistance of $R_0 = 117 \text{ M}\Omega$ at zero bias. Based on the $R_0 A$ value of $46\,800 \Omega \text{ cm}^2$, a detectivity of $D^* = 1.8 \times 10^8$ Jones is estimated at room temperature [54]. The internal quantum efficiency, i.e. the number of electrons generated in the circuit per absorbed photon, is of the order of 14%. It could be enhanced by increasing the doping concentration in the active wells.

In order to test the speed of the device, the detectors have been processed in the form of square 17×17 and $25 \times 25 \mu\text{m}^2$ mesas with hollow top contacts for allowing illumination from their surface [48]. They are electrically contacted using 50Ω coplanar access lines. Figure 10 shows a scanning electron microscope image of a $17 \times 17 \mu\text{m}^2$ mesa QCD. Device fabrication relies on two consecutive etching steps. The first etch down to the bottom AlGaIn layer is used to fabricate the mesas and allow for bottom contacting (region C in figure 10). A second etch down to the sapphire substrate is then performed to remove the doped AlGaIn layer under the access lines (region A in figure 10). The etching was performed in an ICP–RIE system using a dielectric SiO_2 mask and Cl_2/Ar plasma. After the etching steps, the mesas were isolated by Si_3N_4 deposition (region B in figure 10). A Ti/Al/Ti/Au (5/25/15/100 nm) metallization was then performed. The bottom contact was annealed at 650°C and presents an ohmic behavior with a specific contact resistivity of $2 \times 10^{-4} \Omega \text{ cm}^{-2}$.

Photocurrent responsivity was measured in the 0.1–50 GHz frequency range with the device loaded on a 50Ω resistor using an Agilent 86030A lightwave component analyzer (LCA). TM-polarized light excitation was provided by a continuous-wave laser diode at $\lambda = 1.55 \mu\text{m}$. The light was modulated at radio frequency (RF) by a lithium niobate modulator driven by the LCA and further amplified using an erbium-doped fiber amplifier. A polarization-maintaining lensed fiber was used to illuminate the surface of the QCD mesas at 45° angle

of incidence. Microwave probes adapted up to 50 GHz were connected to the coplanar access lines linked to the top and bottom contacts. Figure 10 shows the room-temperature electrical response ($20 \times \log(\text{photocurrent})$) in dB of the 25×25 and $17 \times 17 \mu\text{m}^2$ mesa detectors as a function of the modulation frequency. The curves were normalized at 0 dB at low frequencies. Apart from some instrument-related artifacts around 1–3 GHz, the frequency response of the detectors resembles that of a first-order RC filter with a slope at high frequencies of 20 dB per decade. The -3 dB cut-off frequency is 6.5 GHz for the $25 \times 25 \mu\text{m}^2$ detectors and 11.4 GHz for the $17 \times 17 \mu\text{m}^2$ detectors.

The frequency response of the QCD can be understood by considering its RF equivalent circuit shown in the inset of figure 10. In this scheme, we assume that the QCD behaves as a current source; C_d is the device capacitance, R_c is the access resistance due to the metal contacts and to the resistivity of the AlGaIn contact layers, C_p is the parasitic capacitance between the top and bottom contacts, and L_p is the parasitic inductance that probably results from the junction between the top contact and the access line. The equivalent-circuit elements were extracted by measurement of the S-parameters of the devices using a 50 GHz network analyzer. Simulations show that C_p and L_p would only have a significant impact on the performance at frequencies larger than 150 GHz, i.e. well beyond the currently investigated frequency range. The limiting parameter is the device capacitance, C_d , which is of the order of 97 ± 10 fF for the $25 \times 25 \mu\text{m}^2$. Comparing the two sizes of mesas, C_d roughly scales linearly with the mesa surface area within the error bars. By contrast, the contact resistance only increases by 16% when the mesa size is reduced. Neglecting the parasitic inductance and capacitance, the simulated optical response is that of a first-order filter with a -3 dB cut-off frequency $f_c = 1/(2\pi \times (R_c + R_L)C_d)$. The dotted curves in figure 10 show the fitted optical response for the two sizes of mesa detectors.

It should be noted that the agreement between simulations and measurements of the optical response, and especially the fact that f_c scales with the device area, demonstrates that the speed of the QCDs is governed by the RC filter and not by an intrinsic mechanism. The latter mechanism is the transport time of electrons within the active region. This mechanism should manifest itself as a 40 dB per decade slope of the optical response at large enough frequencies (second-order filter), which is not observed in the experimental measurements within the investigated frequency range. Therefore, we can conclude that intrinsic limitations occur at frequencies above 30 GHz, which gives an upper estimate of the electron transport time of about 5 ps. Considering the energy level diagram, the main intrinsic factor limiting the transport time should be the non-resonant tunneling time between the active QW and the first extractor QW. Indeed, the relaxation of electrons in the extractor should be extremely fast since the energy spacing between the adjacent QW states of the extractor (≈ 100 meV) is close to the energy of the LO-phonon. Based on the internal quantum efficiency, the non-resonant tunneling time is estimated to be ≈ 1 ps [47]. We estimate that the total transport time should be < 1.5 ps, which corresponds to an intrinsic cut-off frequency > 100 GHz. In order to test the intrinsic speed of the QCD, device dimensions and contact resistances must be reduced. One possible design would fabricate a $2 \times 10 \mu\text{m}^2$ waveguide detector in order to benefit from both high speed and enhanced responsivity.

5. Conclusion and prospects

In this paper, we have discussed the specific design of GaN/AlGaIn-based heterostructures for ISB devices. We have shown that by engineering both the electron quantum confinement and

the internal field inherent in the wurtzite structure along the c -axis, it is possible to cover a wide spectral range from near-infrared to mid-infrared. We have also illustrated recent achievements in terms of III-nitride ISB devices operating at telecommunication wavelengths. The first example was an efficient electro-optical modulator exhibiting large modulation depths at room temperature. The second example was a GaN-based QCD, which could provide frequency responses well above 100 GHz. Although the ISB nitride technology is not mature enough to compete with state-of-the-art InP- or GaAs-based technology, rapid progress is being made and some of these devices could find niche applications in various fields of optoelectronics. There are still many challenges facing III-nitride ISB devices. One is the achievement of resonant tunneling, which has so far proved to be elusive probably because of material issues. Another is the demonstration of III-nitride-based ISB lasers, such as the quantum cascade and quantum fountain lasers. It is likely that these latter two devices will first be developed in the THz spectral region in order to benefit from the large energy of the LO-phonons in GaN.

Acknowledgments

This work was supported in part by European FP7 ICT FET-OPEN STREP 'Unitride' under grant agreement no. 233950 and by ANR-06-BLAN-0130 'Transnit'.

References

- [1] West L C and Eglash S J 1985 *Appl. Phys. Lett.* **46** 1156
- [2] Faist J *et al* 1994 *Science* **264** 553
- [3] Tchernycheva M *et al* 2006 *Phys. Rev. B* **73** 125347
- [4] Christense N E *et al* 1994 *Phys. Rev. B* **50** 4397
- [5] Suzuki N and Iizuka N 1997 *Japan. J. Appl. Phys.* **36** L1006
- [6] Gmachl C *et al* 2000 *Appl. Phys. Lett.* **77** 3722
- [7] Kishino K *et al* 2002 *Appl. Phys. Lett.* **81** 1234
- [8] Iizuka N *et al* 2002 *Appl. Phys. Lett.* **81** 1803
- [9] Helman A *et al* 2003 *Appl. Phys. Lett.* **83** 5196
- [10] Gmachl C *et al* 2001 *Appl. Phys. Lett.* **79** 1590
- [11] Tchernycheva M *et al* 2006 *Appl. Phys. Lett.* **88** 153113
- [12] Driscoll K *et al* 2007 *Appl. Phys. Lett.* **91** 141104
- [13] Nicolay S *et al* 2005 *Appl. Phys. Lett.* **87** 111106
- [14] Cywinski G *et al* 2006 *J. Vac. Sci. Technol. B* **2** 1505
- [15] Moumanis K *et al* 2003 *Appl. Phys. Lett.* **82** 868
- [16] Tchernycheva M *et al* 2005 *Appl. Phys. Lett.* **87** 101912
- [17] Guillot F *et al* 2006 *J. Appl. Phys.* **100** 044326
- [18] Grandjean N 2009 private communication
- [19] Monroy E *et al* 2008 *J. Mater. Sci.* **19** 821
- [20] Waki I *et al* 2004 *Appl. Phys. Lett.* **84** 3703
- [21] Nicolay S *et al* 2006 *Appl. Phys. Lett.* **88** 151902
- [22] Mosca M *et al* 2007 *Phys. Status Solidi a* **204** 1100
- [23] Nicolay S *et al* 2007 *Appl. Phys. Lett.* **91** 061927
- [24] Iizuka N *et al* 2000 *Appl. Phys. Lett.* **77** 648
- [25] Heber J D *et al* 2002 *Appl. Phys. Lett.* **81** 1237
- [26] Hamazaki J *et al* 2004 *Appl. Phys. Lett.* **84** 1102

- [27] Iizuka N *et al* 2005 *Opt. Exp.* **13** 3835
- [28] Li Y *et al* 2007 *Opt. Exp.* **15** 17922
- [29] Hofstetter D *et al* 2003 *Appl. Phys. Lett.* **83** 572
- [30] Baumann E *et al* 2005 *Appl. Phys. Lett.* **87** 191102
- [31] Hofstetter D *et al* 2007 *Appl. Phys. Lett.* **91** 131115
- [32] Doyennette L *et al* 2005 *Electron. Lett.* **41** 1077
- [33] Vardi A *et al* 2006 *Appl. Phys. Lett.* **88** 143101
- [34] Baumann E *et al* 2006 *Appl. Phys. Lett.* **89** 101121
- [35] Nevou L *et al* 2007 *Appl. Phys. Lett.* **90** 223511
- [36] Kheirodin N *et al* 2008 *IEEE Photon. Technol. Lett.* **20** 724
- [37] Iizuka N *et al* 2006 *J. Appl. Phys.* **99** 0913107
- [38] Lupu A *et al* 2008 *IEEE Photon. Technol. Lett.* **20** 102
- [39] Nevou L *et al* 2006 *Electron. Lett.* **42** 1308
- [40] Nevou L *et al* 2007 *Appl. Phys. Lett.* **90** 121106
- [41] Nevou L *et al* 2008 *Phys. Status Solidi c* **5** 2120
- [42] Driscoll K *et al* 2009 *Appl. Phys. Lett.* **94** 081120
- [43] Julien F H *et al* 2007 *Phys. Status Solidi a* **204** 1987
- [44] Nevou L *et al* 2008 *Appl. Phys. Lett.* **92** 161105
- [45] Nevou L *et al* 2006 *Appl. Phys. Lett.* **89** 151101
- [46] Valdueza-Felip S *et al* 2008 *IEEE Photon. Technol. Lett.* **20** 1366–8
- [47] Vardi A *et al* 2008 *Appl. Phys. Lett.* **92** 011112
- [48] Vardi A *et al* 2008 *Appl. Phys. Lett.* **93** 193509
- [49] Vurgaftman I and Meyer J R 2003 *J. Appl. Phys.* **94** 3675
- [50] Bernardini F and Fiorentini V 1998 *Phys. Rev. B* **57** R9427
- [51] Leroux M *et al* 1998 *Phys. Rev. B* **58** R13371
- [52] Kandaswamy P K *et al* 2008 *J. Appl. Phys.* **104** 093501
- [53] Kandaswamy P K *et al* 2009 *Appl. Phys. Lett.* **95** 141911
- [54] Lahourcade L *et al* 2008 *Appl. Phys. Lett.* **93** 111906
- [55] DeCuir E A *et al* 2008 *Appl. Phys. Lett.* **92** 201910
- [56] Holmström P 2006 *IEEE J. Quantum Electron.* **42** 810
- [57] Gendron L *et al* 2004 *Appl. Phys. Lett.* **85** 2824
- [58] Gomez A *et al* 2008 *Phys. Rev. B* **77** 085307
- [59] Giorgetta F R *et al* 2007 *Appl. Phys. Lett.* **91** 111115